Highly tunable propagating surface plasmons on supported silver nanowires

Hong Wei[a], Shunping Zhang[a], Xiaorui Tian[a], and Hongxing Xu[a,b,c,1]

[a]Beijing National Laboratory for Condensed Matter Physics and Institute of Physics, Chinese Academy of Sciences, Beijing 100190, China; [b]Center for Nanoscience and Nanotechnology, and School of Physics and Technology, Wuhan University, Wuhan 430072, China; and [c]Division of Solid State Physics/The Nanometer Structure Consortium, Lund University, S-22100 Lund, Sweden

Surface plasmons, the quanta of the collective oscillations of free electrons at metal surface, can be easily tuned by changing the surrounding dielectric materials, which is well known for metal nanoparticles and metal surfaces, but less is known for one-dimensional metal nanowires. Here, we find an extremely large tunability of surface plasmons on Ag nanowires with a beat period of the near-field distribution pattern increasing by 90 nm per nanometer of Al_2O_3 coating, or by 16 µm per refractive index unit change in the surrounding medium. Such high sensitivity is crucial to directly control the optical signal distribution for various routing and demultiplexing functions in plasmonic circuits and may pave the way to the development of on-chip ultrasensitive biosensing.

plasmonics | imaging | sensing | quantum dot | modulation

The miniaturization of optical devices to the scale compatible with modern nanoelectronic circuits demands the ability to manipulate light at the subwavelength scale. Recently, plasmonics has been a rapidly emerging field that offers various means to manipulate light at the nanometer scale using surface plasmons (SPs) (1–10). SPs can strongly confine electromagnetic fields near metal–dielectric interface to overcome the conventional diffraction limit of dielectric optics. Therefore, SP-based nanophotonic devices are promising to build densely on-chip integrated circuits for next-generation information technology (11, 12). The scaling down of photonic circuits may find applications in quantum information processing as well (13, 14). It is known that the properties of SPs can be strongly affected by the surrounding dielectric materials, e.g., the refractive index of the surrounding material determines the dispersion relations and resonance energies of SPs (15). Although the sensitivity of localized SPs on various metal nanostructures to local dielectric environments has been well studied, less is known for the cases of propagating SPs in plasmonic circuits. It is a challenge to develop advanced plasmonic modulation schemes for designing simple, robust metal–dielectric heteronanostructures suitable for high-performance on-chip plasmonic circuits.

Plasmonic waveguide is one of the key elements for the plasmonic circuits. Different nanostructures have been investigated as waveguides (16–24). Chemically synthesized crystalline silver nanowires (Ag NWs) can support propagating SPs (25–28) with lower losses than lithographically defined NW waveguides (29), and can be easily manipulated to construct complex optical devices (30–33), which make them ideal candidates for proof-of-principle studies of plasmonic circuits. Metal NWs of diameters of tens to hundreds of nanometers and lengths of several to tens of micrometers are mesoscopic systems, which show many novel and valuable properties and may potentially be used in many fields. To investigate the SP propagating properties in metal NWs, both near-field optical microscopy and quantum dots (QDs) fluorescence imaging where QDs are used as local field reporters were applied to produce optical images of plasmon-induced near-field distributions on Ag NWs (29, 32, 34). Near-field distributions of propagating NW plasmons depend strongly on the polarization and phase of the input light, which can be

used to realize an entire family of optical Boolean logic gates in NW networks (32). Despite the developments of plasmonic circuits, the key issue is still on how to exactly control and route optical signals in various circuitries with simple design principles. Here, we discover an extremely large tunability of propagating SP near-field pattern on Ag NWs using the QD fluorescence imaging technique. Locally changing the dielectric environment by applying a thin dielectric coating layer of Al_2O_3 results in the period increasing by about 90 nm per nanometer of Al_2O_3. For bulk changes in the surrounding medium, we observe a period increase of about 16 µm per refractive index unit. This high-sensitivity effect is explained by considering the propagation constants and the dispersion curves of NW SPs. We demonstrate that such giant modulation of SPs can be used to design functional plasmonic circuits.

Results

Influence of Dielectric Environment to the Near-Field Distribution Pattern. The structure considered here, illustrated in Fig. 1*A*, consists of Ag NWs of radius R deposited on a glass substrate, and coated with dielectric (Al_2O_3) layers of different thicknesses T and a layer of QDs surrounded by a medium. The laser light was focused through an objective onto one end of the NW and the signal was collected by the same objective. After filtering the laser light, QD fluorescence was recorded by a CCD camera (illustrated in Fig. 1*B*; see *Methods* for more details). A HeNe laser operating at a wavelength of 633 nm was used for SP excitation unless specified. Scanning electron microscope (SEM) images of typical NW structures are shown in Fig. 1*C*, where the smooth Al_2O_3 coating is clearly resolved.

Fig. 1 *D–F* show typical QD emission images revealing a quasiperiodic oscillation of the near field with a period (Λ) that is highly sensitive to local or bulk changes of the surrounding dielectric materials. In Fig. 1*D*, Λ increases dramatically with the thickness T of the Al_2O_3 coating: for $T = 30$ nm (*Top*) $\Lambda \sim 1.7$ µm, increasing to 2.9 µm for $T = 50$ nm (*Middle*), and 5.8 µm for $T = 80$ nm (*Bottom*). This high sensitivity to small changes in T is further demonstrated in Fig. 1*E* where 50 nm of Al_2O_3 was initially deposited on a NW followed by a layer of QDs, and then additional Al_2O_3 in 5-nm increments. Initially, this NW shows a near-field beat period of 2.9 µm (Fig. 1*E*, *Top*), increasing to 3.3 µm (*Middle*) when just 5 nm of Al_2O_3 is added, and to 3.8 µm with an additional 5 nm (*Bottom*). This corresponds to Λ increasing $\sim$90 nm when the coating thickness is increased 1 nm. It is interesting that such an increase to each period is cumulative along the NW to make an enormous shift of the last period as $N \cdot \Delta \Lambda$,
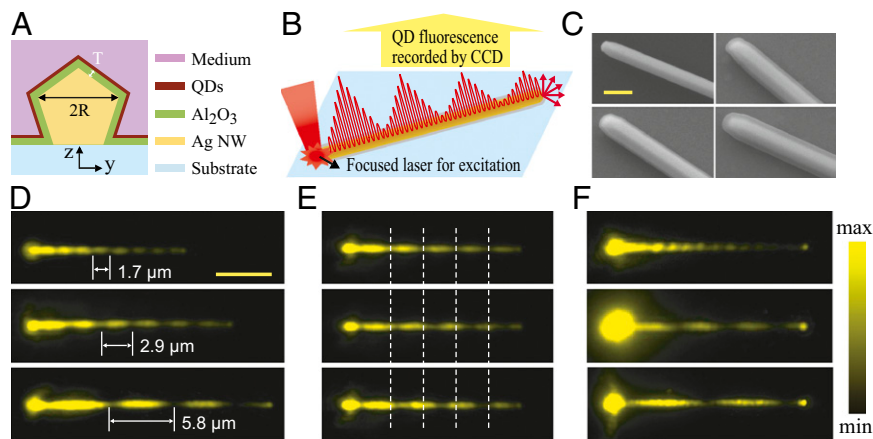
Fig. 1. Near-field distribution images for NWs with different dielectric environments. (*A*) Schematic cross-section of the samples. (*B*) Schematic illustration of the excitation/collection configuration and the plasmons propagating along the NW. (*C*) SEM images of a typical bare Ag NW (*Upper Left*) and NWs coated with $T = 30$ nm (*Lower Left*), 50 nm (*Upper Right*), and 80 nm (*Lower Right*) Al_2O_3 layers. (Scale bar, 500 nm.) (*D*) QD emission images under excitation at the left ends of the NWs. From *Top* to *Bottom*, the radius of the NWs is 160, 155, and 157 nm, and the corresponding Al_2O_3 thicknesses are 30, 50, and 80 nm. (*E*) QD emission images for a 162-nm radius NW with a 50-nm Al_2O_3 coating measured in air (*Top*), and then after depositing 5 nm of Al_2O_3 (*Middle*), and finally with an additional 5 nm of Al_2O_3 (*Bottom*). The white dashed lines are visual guides to show the shift of the plasmon near-field pattern. (*F*) QD emission images for a 155-nm radius NW initially coated with 10 nm of Al_2O_3 and QDs, and then capped with another 5 nm of Al_2O_3 to protect the water-soluble QDs from being removed, measured in air (*Top*), water (*Middle*), and oil (*Bottom*). (Scale bar in D for D–F, 5 μm.)

where N is the number of total periods. Comparing Fig. 1*E Top* and *Bottom* shows that the shift of the last null after depositing an additional 10 nm of Al_2O_3 is 3.6 μm, i.e., ~360 nm per nanometer of Al_2O_3. Another example with similar high sensitivity of the near-field beat pattern starting from $T = 30$ nm is shown in Fig. S1.

Immersing the samples in water or oil rather than in air, increasing the refractive index n of the surrounding medium from 1.00 to 1.33 or 1.51, respectively, dramatically changes the near-field pattern as shown in Fig. 1*F*. In Fig. 1*F*, Λ increases rapidly from 1.3 μm in air to 4.4 μm in water and 7.2 μm in oil. Expressed as a change in period per refractive index unit (RIU), this corresponds to $\Delta\Lambda/\Delta n = 9.4$ μm/RIU from air to water and 16 μm/ RIU from water to oil. The total sensitivity of the whole NW will cumulate the sensitivity of each period to be $N\cdot\Delta\Lambda/\Delta n$, where N is the number of total periods. For the case of Fig. 1*F*, the corresponding sensitivity becomes 3×9.4 μm/RIU = 28.2 μm/RIU from air to water and 2×16 μm/RIU = 32 μm/RIU from water

to oil, respectively. Due to such cumulation effect, in principle, much larger sensitivity can be obtained for longer NWs.

Plasmon Beating and the Mechanism for the High Sensitivity. Because the chemically synthesized Ag NWs used here have pentagonal cross-section (35), we used pentagonal wires in the simulation to mimic the real situation. For cylindrical NW, plasmon modes are usually indexed with quantum number "m," as $|m| = 0, 1, 2,...$ (36, 37). However, here, both the pentagonal shape and the interaction to the dielectric substrate break the perfect symmetry of the cylindrical shape in an ideal system, and "m" is not a good index anymore. As shown in Fig. 2*A*, three lowest-order SP modes for a coated NW ($R = 110$ nm, $T = 80$ nm) on a glass substrate are denoted as H_0, H_1, and H_2. The field distributions of these three modes are obtained from a finite element method (FEM) package (COMSOL Multiphysics 3.5a). To model such large system involving substrate, we performed 3D electrodynamics calculations using another commercial software (Lumerical Solution) based on
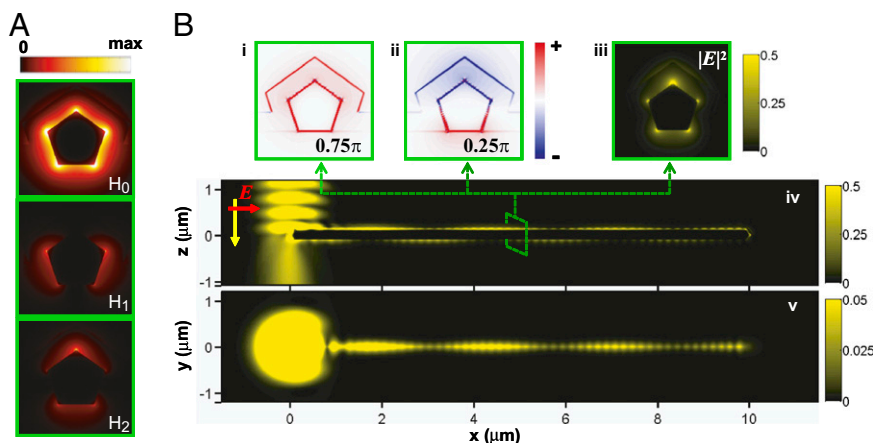
Fig. 2. Excitation of multiple SP modes on supported NWs. (*A*) Power distribution of three lowest-order modes on supported NW. (*Bi* and *Bii*) Charge plot with different initial phase, 0.75π and 0.25π; (*Biii–Bv*) electric field intensity $|E|^2$ distribution on different cross-section of the Ag NW, excited by a Gaussian beam at the left end. The *yz* plot (*Biii*)/*xz* plot (*Biv*) is cut through the wire at $x = 5.0$ μm/$y = 0$ μm, and the *xy* plot is located 10 nm above the coated NW. The radius of the wire is $R = 110$ nm, and the coating thickness is $T = 80$ nm. The incident light, $\lambda = 632.8$ nm, is polarized parallel to the wire axis in B.

finite difference time-domain (FDTD) method, as shown in Fig. 2B. For the calculations in Fig. 2B, the laser beam is polarized parallel to the NW. The charge plots in Fig. 2 Bi and Bii and the electric field intensity distribution in Fig. 2Biii clearly reveal that both the H_0 and H_2 modes are excited. The coherent interference of the H_0 and H_2 mode generates plasmon beating along the NW, as shown in Fig. 2 Biv and Bv. The period of the beating is given by $\Lambda = 2\pi/Re(\Delta k_{//})$, where $\Delta k_{//}$ is the difference of the propagation constant of the H_0 and H_2 mode. The oscillations with a short period are due to the interference between counterpropagating SPs resulting from reflections by the two terminals of the NW, i.e., Fabry–Pérot resonances (29), which is dependent on the length of the wire. The plasmon beating, however, can exist as long as both of the modes are not damped out, independent of the NW length. Because the H_1 mode is not excited in the current configuration, it will not be discussed in the following, but the perpendicular components of the incident electric field to the wire axis, i.e., the change of the incident polarization, can excite H_1 mode and higher-order modes as can be seen in Fig. S2.

We experimentally measured the beat period of coated NWs of varying radius R and coating thickness T. From Fig. 3A, we can see that the beat period Λ increases with increasing R, and also with increasing T. For the NWs with thick coating ($T = 80$ and 100 nm), Λ is increased monotonically with the increase of the NW radius, which is reproduced by the calculation. This phenomenon can be explained by the decrease of $Re(\Delta k_{//})$ with the increase of the NW radius as seen in Fig. 3B. For the NWs with thin coating ($T \leq 50$ nm), the increase in Λ with radius saturates for R greater than ~125 nm. Because the propagation constant $Re(k_{//})$ of the H_2 mode cannot be obtained by our FEM model for NWs with thinner coating because the mode becomes leaky in this case, a reproduction of the measured beat periods for thin coating was then done using 3D FDTD calculations, as shown in Fig. S3. For very thin wires ($R < 50$ nm), the interference pattern disappears as the

H_2 mode becomes difficult to excite, whereas for wires of larger radiuses ($R > 200$ nm), higher-order SP modes are also excited so that the quasiperiodic near-field distributions become ill defined (Fig. S4).

We extract some data from Fig. 3A to show Λ versus T in Fig. 3C. It is clear that Λ increases at the beginning and becomes saturated for larger T. This result is consistent with the calculated data obtained from the real part of the propagation constant $Re(k_{//})$. As can be seen from Fig. 3D, the change of the real part of the propagation constant $Re(k_{//})$ is larger for the H_2 mode than the H_0 mode as the thickness of the Al_2O_3 coating T is varied. That is because for a bare NW on top of a dielectric substrate, i.e., without Al_2O_3 coating, the field of the H_0 mode is located at the bottom of the wire, whereas that of the H_2 mode is on the top of the wire (38). As a result, the dielectric screening effect will be more pronounced for the H_2 mode than for the H_0 mode. With the adding of the Al_2O_3 coating onto the NW, the difference between the propagation constant of the H_0 and the H_2 mode becomes smaller. Therefore, the beat period becomes larger. However, increasing the thickness of Al_2O_3 layer tends to reduce the coupling to the substrate because the NW feels a more symmetric dielectric environment for very thick coatings. The increase of the real parts of the propagation constants $Re(k_{//})$ of H_1 and H_2 mode becomes saturated when the thickness of Al_2O_3 layer is very thick, which makes the beat period Λ stop increasing and saturate to a value corresponding to the infinite coating thickness. Fig. S5 shows the calculated $Re(k_{//})$ of the H_0 and H_2 mode for larger Al_2O_3 coating thickness. For NWs in a homogenous environment, Λ increases monotonically with R as shown in Fig. S6, which is demonstrated in the experimental results measured in oil (Fig. S7).

To better understand the physical mechanism of the plasmon beating behavior observed in the experiment and reproduced in the calculation, we examine the dispersion relation for

Fig. 3. (A and B) The beat period (A) and the real part of the propagation constant $Re(k_{//})$ of the H_0 and H_2 mode (B) as a function of NW radius. (C and D) The beat period (C) and $Re(k_{//})$ of the H_0 and H_2 mode (D) as a function of Al_2O_3 coating thickness. The NW radius is 155 nm for the calculation in D. In A and C, the dots are experimental data, and the lines are FEM calculated data.

Fig. 4. Dispersion relations for the $m = 0$ (solid) and $|m| = 1$ (dash) plasmon modes of a bare Ag NW in air (black) and in glass matrix (blue), and the H_0 and H_2 modes (red) of a NW supported on air–glass interface. The NW (radius $R = 150$ nm) has a cylindrical cross-section.

propagating NW SPs. For simplicity, cylindrical NWs are used to obtain the dispersion relation data. The black curves in Fig. 4 show the dispersion relations for the $m = 0$ (black solid curve) and for the $|m| = 1$ (black dashed curve) SPs on a bare NW of radius 150 nm in a symmetric dielectric environment (air). When the NWs are deposited on a substrate, the dielectric environment is highly asymmetric. The induced charge on the substrate surface caused by the oscillating charges of different SP modes will change the charge distributions of the primary modes $|m| = 0$, 1,... to form the asymmetric H_0, H_1, and H_2,... modes and shift the corresponding dispersion relations. Similar to the coupling between two close-packed metal NWs (39), here the wire on the substrate is coupled to its "image" wire in the substrate, and the dispersion relation of the lowest-order mode, i.e., $m = 0$, will be dramatically red-shifted due to the strong "monopole" coulomb coupling to the substrate. The dispersion relations of the higher-order modes ($|m| = 1, 2,...$) will be influenced as well, but the corresponding "multipole" couplings decrease with the coupling coulomb potential proportional to $\sim r^{-(2m+1)}$, where r is the effective distance between two multipole sources, resulting in a less dramatic red shift of the dispersion relation compared with the lowest-order mode. Hence, the substrate-mediated interaction will increase $\mathrm{Re}(\Delta k'_{//}) = \mathrm{Re}(k_{0//}') - \mathrm{Re}(k_{1//}')$ as shown by the red curves in Fig. 4, resulting in a smaller beat period Λ on the substrate (comparing Fig. S6 and Fig. 3A). With increasing thickness of a refractive index-matched coating layer, however, the substrate-mediated interaction will be decreased, and the dielectric screening effect caused by the coating layer will shift the dispersion curves of both H_0 and H_2 to red, but a much faster shift for H_2 mode as seen in Fig. 3D, resulting in a smaller difference between the propagation constants of the two modes. Thus, the beat period Λ is increased with the increase of the coating thickness and saturates for very thick coatings due to the more symmetric dielectric environment. A reduction of the asymmetry can also occur if the air medium is replaced by a medium that more closely index-matches the substrate on which the wires are placed, which is what is observed in Fig. 1F. The blue curves in Fig. 4 show the dispersion relations for the two lowest-order modes on a NW embedded in the glass matrix with a smaller $\mathrm{Re}(\Delta k''_{//})$.

Near-Field Distribution Dependence on the Excitation Wavelength and Its Application in Plasmonic Circuits. The QDs also fluoresce when excited with a laser of 532-nm wavelength, allowing us to study the effect of excitation wavelength on the beat period. For

NWs with $T = 30$ nm, Λ is similar for both 633- and 532-nm excitation (Fig. 5 A and B), whereas for NWs with $T = 50$ nm, Λ is larger when excited by 532-nm light (Fig. 5 C and D). It is noted that the change of the beat period is most sensitive to the change of the thickness of the coating layer at about $T = 50$ nm in Fig. 3C for the excitation by laser light of 633-nm wavelength. The larger increase of the period for 532-nm excitation indicates that the sensitivity to the change of the Al_2O_3 coating thickness is higher for 532-nm excitation than 633-nm excitation in the thickness range considered here. From these results, we can also see that how strongly Λ depends on excitation wavelength can be controlled through the geometry. This flexibility is important for engineering plasmonic circuits where it may be desired to keep signals at different wavelengths together or separate them to follow different paths depending on the device function.

To demonstrate how the highly tunable near-field distribution plays an important role in plasmonic devices and circuits, we designed a structure composed of three NWs (Fig. 6A, Left) and coated it with 30-nm Al_2O_3. By adding additional Al_2O_3 in 5-nm increments, we demonstrate that small changes in the coating layer can control the routing of light to different terminals of the device. A supercontinuum light source was used for excitation of propagating plasmons (Fig. 6A, Right), which enables us to study the wavelength response of the structure. The spectrum of the output light at terminal A for the initial structure (black curve in upper panel of Fig. 6B) shows that the transmission of light to terminal A is much higher at wavelengths around 633 and 820 nm compared with 700 nm. The spectrum at terminal B (black curve in lower panel of Fig. 6B) shows similar behavior. Depositing an additional 5 nm of Al_2O_3 results in the output intensity increasing at both terminals A and B across most of the spectrum (red curves in the upper and lower panels of Fig. 6B, respectively). For terminal A, there is a striking increase in the output around 633 nm so that the output around 633 and 800 nm is now equal. Adding an additional 5 nm of Al_2O_3 results in opposite behavior at terminals A and B (blue curves): for terminal A the output

Fig. 5. Near-field distribution for different excitation wavelengths. (A) QD emission images for a 140-nm radius NW coated with 30 nm of Al_2O_3 for an excitation wavelength of 633 nm (Upper) and 532 nm (Lower). (B) The intensity profiles along the NW between the short bars in A, which are obtained by plotting the intensity of single pixels along the NW as a function of the distance. The intensity is normalized by the maximum of the two curves. (C and D) The corresponding data for a 135-nm radius NW coated with 50 nm of Al_2O_3. (Scale bars, 5 μm.)

Fig. 6. Control the output by controlling the near-field distribution. (*A*) A structure composed of three NWs was illuminated by the supercontinuum light with the incident polarization parallel to the main NW. (*B*) The upper panel shows the emission spectra at the terminal A from the right branch for the original structure (black), and for 5 nm (red) and 10 nm (blue) Al_2O_3 layer deposited, respectively. The lower panel is for the terminal B from the left branch. (*C*) The QD emission images when excited with a laser of 633-nm wavelength for the original structure (*Left*) and after 5 nm more Al_2O_3 was deposited (*Right*). The red dashed lines in *A* and *C* show the positions of two branch wires. The white dashed line in *C* is a visual guide to show the shift of the near-field nodes and antinodes due to the addition of 5 nm of Al_2O_3. The batch of NWs used for this structure has the radius of about 150 nm. (Scale bar in *A*, 5 μm.)

decreases dramatically around 800 nm and only light around 633 nm is strongly coupled to this terminal, whereas for terminal B the transmission around 800 nm is unaffected and the transmission around 633 nm is suppressed. The images of QD fluorescence excited by a laser of 633 nm in Fig. 6*C* show that the plasmon antinode moves to the junction position of the right branch (marked by red dashed line) when the first 5 nm of Al_2O_3 was deposited, which make more light be routed to this branch wire. This observation agrees well with the spectral intensity change in Fig. 6*B*. These results demonstrate that the tunable plasmon near-field distribution plays a critical role in determining the path light follows through plasmonic circuits.

Discussion

We have found extremely large modulation of the near-field distribution of SPs on supported Ag NWs by slightly changing the surrounding dielectric environment. This effect can be understood by examining the dispersion properties of the NW SPs, which are highly sensitive to the change of the surroundings. Such high sensitivity has been demonstrated to design plamonic devices with different routing functions in NW networks by slightly changing the dielectric coating thickness here. This discovery of large tunability of the propagating SPs on Ag NW networks thus provides a simple and robust way for the exact control of plasmon near-field distributions and the precise routing of optical signals in circuitries. Based on the mechanism revealed here, active plasmonic devices can also be designed with carefully selected electro-optical and optical nonlinear coating materials (40, 41). The current study can give the design principle for both passive and active plasmonic devices, which will promote the development of on-chip integrated plasmonic circuits.

Such highly tunable near-field distribution on supported Ag NWs can also be used for new types of ultrasensitive on-chip optical sensors. The dramatic change of the beat period demonstrated here can be caused by the adsorption of tiny amount of molecules on the metal NWs, for example, which changes the local dielectric environment. More importantly, the change of the beat period will cumulate with each period to largely change the position of the last period, and the corresponding total sensitivity will be enlarged for longer wires with more periods. As demonstrated here, the cumulated change ~360 nm per nanometer of Al_2O_3 coating of the last node position after four-period accumulation, roughly corresponding to a monolayer of small biomolecule adsorption, can be resolved by the ordinary confocal microscopy. By applying the advantages of scanning near-field optical microscopy with the resolution about 10 nm (42, 43), together with longer wires with more beat periods used, hundred times higher sensitivity can be achieved. Hence, ultrasensitive wire plasmon sensors based on the principle discussed here can be developed. In addition, the dramatic changes of the emission spectra and the shift of the fine fringes on the spectra due to Fabry–Pérot resonances (Fig. 6*B*) can also be used for highly sensitive sensing applications.

Methods

Sample Preparation. The Ag NWs were prepared by reducing silver nitrate with ethylene glycol in the presence of poly(vinyl pyrrolidone) (44) and washed in ethanol via centrifugation. The Ag NW suspension in ethanol was then deposited on glass slides. Al_2O_3 layers were grown on the NWs using an atomic layer deposition (ALD) system (Cambridge NanoTech; Savannah-100) operating at 200 °C. ZnS-coated CdSe QDs (Invitrogen; Catalog number Q21321MP) were diluted in highly purified water, and then spin-coated on the Al_2O_3 layer. Additional layers of Al_2O_3 may be deposited on top of the QD layer to investigate the effect of small changes in the thickness of the dielectric coating or to protect the QD layer for measurements in a liquid environment. For the deposition of Al_2O_3 on top of the QDs, the ALD system is operated at 80 °C.

Optical Measurements. Optical measurements were performed using two different but functionally equivalent microscope systems. The optical imaging measurements for Figs. 1 and 5 were performed using an Olympus BX 51 microscope. A 100× objective (N.A. 0.95) was used for excitation and collection of the images measured in air. A 100× objective (N.A. 1.35) and

a 60× objective (N.A. 1.2) were used for the measurements in oil and water. For the imaging of the near-field distribution of propagating SPs, a HeNe laser operating at a wavelength of 633 nm or a frequency-doubled Nd:YAG laser for 532 nm was used for excitation at the NW termini. The QD emission images were recorded by a CCD camera (DVC-1412 AM) after the emitted light was transmitted through a long-pass edge filter to block the excitation laser. For Fig. 3A, a Leica DM LM microscope with a 50× (N.A. 0.75) or 100× (N.A. 0.85) objective attached to a Renishaw inVia microRaman system were used to collect optical imaging data. A HeNe laser for 633 nm was used for excitation at the NW termini, and the QD emission imaging data were recorded with a CCD camera (Renishaw RenCam) after the emitted light passed through two long-pass edge filters and a narrow bandpass filter to block the excitation laser and select the QD emission. For Fig. 6B, a super-continuum light source (Fianium; SC400-PP) was used for excitation through a 100× (N.A. 0.9) objective on an Olympus BX 51 microscope. The output light at NW terminals was directed to a spectrometer (Princeton Instruments; Acton SP-2560) to measure the spectra.

Simulations. The mode profiles in Fig. 2A and their propagation constants were obtained using the mode solver in COMSOL. These mode analyses were done in the 2D cross-section of the pentagonal NWs. Full-wave electromagnetic simulations were performed using FDTD software (Lumerical Solution). The model used in the calculations is the same as in Fig. 1A, except the QD

layer is omitted, and the structural parameters R and T are determined from the experiments. The simulation domain boundaries were extended no less than 1.35 μm away from the wire and perfectly matched layers were used to mimic an infinite substrate and infinite upper half space. A focused Gaussian beam is inserted perpendicular to the wire axis at one of the wire ends. The refractive index of the Al_2O_3 layer and the glass substrate was assumed to be 1.62 and 1.50, respectively. The dielectric permittivity for Ag ($\varepsilon_{Ag} = -18.36 + 0.48i$) was taken from Johnson and Christy (45), corresponding to the vacuum wavelength $\lambda = 632.8$ nm. The charge plots in Fig. 2 Bi and Bii were done numerically by calculating the real part of the divergence of the electric field $\text{Re}(\nabla \cdot \boldsymbol{E} \cdot e^{i\varphi})$, where φ represents the initial phase. The dispersion curves of the NW SP modes in Fig. 4 were obtained using the mode solver in the COMSOL multiphysics finite element modeling package.

1. Barnes WL, Dereux A, Ebbesen TW (2003) Surface plasmon subwavelength optics. *Nature* 424(6950):824–830.
2. Schuller JA, et al. (2010) Plasmonics for extreme light concentration and manipulation. *Nat Mater* 9(3):193–204.
3. Lee SJ, Guan ZQ, Xu HX, Moskovits M (2007) Surface-enhanced Raman spectroscopy and nanogeometry: The plasmonic origin of SERS. *J Phys Chem C* 111(49):17985–17988.
4. Shegai T, et al. (2008) Managing light polarization via plasmon-molecule interactions within an asymmetric metal nanoparticle trimer. *Proc Natl Acad Sci USA* 105(43):16448–16453.
5. Schnell M, et al. (2009) Controlling the near-field oscillations of loaded plasmonic nanoantennas. *Nat Photonics* 3(5):287–291.
6. Zhang WH, Huang LN, Santschi C, Martin OJF (2010) Trapping and sensing 10 nm metal nanoparticles using plasmonic dipole antennas. *Nano Lett* 10(3):1006–1011.
7. Zhang JT, Tang Y, Lee K, Ouyang M (2010) Tailoring light-matter-spin interactions in colloidal hetero-nanostructures. *Nature* 466(7302):91–95.
8. MacDonald KF, Samson ZL, Stockman MI, Zheludev NI (2009) Ultrafast active plasmonics. *Nat Photonics* 3(1):55–58.
9. Juan ML, Righini M, Quidant R (2011) Plasmon nano-optical tweezers. *Nat Photonics* 5(6):349–356.
10. Bharadwaj P, Bouhelier A, Novotny L (2011) Electrical excitation of surface plasmons. *Phys Rev Lett* 106(22):226802.
11. Ozbay E (2006) Plasmonics: Merging photonics and electronics at nanoscale dimensions. *Science* 311(5758):189–193.
12. Maier SA, Atwater HA (2005) Plasmonics: Localization and guiding of electromagnetic energy in metal/dielectric structures. *J Appl Phys* 98(1):011101.
13. Peruzzo A, Laing A, Politi A, Rudolph T, O'Brien JL (2011) Multimode quantum interference of photons in multiport integrated devices. *Nat Commun* 2:224.
14. Shadbolt PJ, et al. (2012) Generating, manipulating and measuring entanglement and mixture with a reconfigurable photonic circuit. *Nat Photonics* 6(1):45–49.
15. Mayer KM, Hafner JH (2011) Localized surface plasmon resonance sensors. *Chem Rev* 111(6):3828–3857.
16. Dickson RM, Lyon LA (2000) Unidirectional plasmon propagation in metallic nanowires. *J Phys Chem B* 104(26):6095–6098.
17. Lamprecht B, et al. (2001) Surface plasmon propagation in microscale metal stripes. *Appl Phys Lett* 79(1):51–53.
18. Pile DFP, Gramotnev DK (2004) Channel plasmon-polariton in a triangular groove on a metal surface. *Opt Lett* 29(10):1069–1071.
19. Pile DFP, et al. (2005) Theoretical and experimental investigation of strongly localized plasmons on triangular metal wedges for subwavelength waveguiding. *Appl Phys Lett* 87(6):061106.
20. Bozhevolnyi SI, Volkov VS, Devaux E, Laluet JY, Ebbesen TW (2006) Channel plasmon subwavelength waveguide components including interferometers and ring resonators. *Nature* 440(7083):508–511.
21. Zia R, Schuller JA, Brongersma ML (2006) Near-field characterization of guided polariton propagation and cutoff in surface plasmon waveguides. *Phys Rev B* 74(16):165415.
22. Spasenovic M, van Oosten D, Verhagen E, Kuipers L (2009) Measurements of modal symmetry in subwavelength plasmonic slot waveguides. *Appl Phys Lett* 95(20):203109.
23. Chen XW, Sandoghdar V, Agio M (2009) Highly efficient interfacing of guided plasmons and photons in nanowires. *Nano Lett* 9(11):3756–3761.
24. Smith EJ, Liu ZW, Mei YF, Schmidt OG (2010) Combined surface plasmon and classical waveguiding through metamaterial fiber design. *Nano Lett* 10(1):1–5.
25. Sanders AW, et al. (2006) Observation of plasmon propagation, redirection, and fanout in silver nanowires. *Nano Lett* 6(8):1822–1826.
26. Wei H, Ratchford D, Li XE, Xu HX, Shih CK (2009) Propagating surface plasmon induced photon emission from quantum dots. *Nano Lett* 9(12):4168–4171.
27. Li ZP, et al. (2010) Effect of a proximal substrate on plasmon propagation in silver nanowires. *Phys Rev B* 82(24):241402.
28. Fang ZY, et al. (2011) Plasmonic coupling of bow tie antennas with Ag nanowire. *Nano Lett* 11(4):1676–1680.
29. Ditlbacher H, et al. (2005) Silver nanowires as surface plasmon resonators. *Phys Rev Lett* 95(25):257403.
30. Fang YR, et al. (2010) Branched silver nanowires as controllable plasmon routers. *Nano Lett* 10(5):1950–1954.
31. Yan RX, Pauzauskie P, Huang JX, Yang PD (2009) Direct photonic-plasmonic coupling and routing in single nanowires. *Proc Natl Acad Sci USA* 106(50):21045–21050.
32. Wei H, et al. (2011) Quantum dot-based local field imaging reveals plasmon-based interferometric logic in silver nanowire networks. *Nano Lett* 11(2):471–475.
33. Guo X, et al. (2009) Direct coupling of plasmonic and photonic nanowires for hybrid nanophotonic components and circuits. *Nano Lett* 9(12):4515–4519.
34. Wei H, Wang ZX, Tian XR, Käll M, Xu HX (2011) Cascaded logic gates in nanophotonic plasmon networks. *Nat Commun* 2:387.
35. Sun YG, Mayers B, Herricks T, Xia YN (2003) Polyol synthesis of uniform silver nanowires: A plausible growth mechanism and the supporting evidence. *Nano Lett* 3(7):955–960.
36. Chang DE, Sorensen AS, Hemmer PR, Lukin MD (2007) Strong coupling of single emitters to surface plasmons. *Phys Rev B* 76(3):035420.
37. Zhang SP, et al. (2011) Chiral surface plasmon polaritons on metallic nanowires. *Phys Rev Lett* 107(9):096801.
38. Zhang SP, Xu HX (2012) Optimizing substrate-mediated plasmon coupling toward high-performance plasmonic nanowire waveguides. *ACS Nano* 6(9):8128–8135.
39. Manjavacas A, García de Abajo FJ (2009) Robust plasmon waveguides in strongly interacting nanowire arrays. *Nano Lett* 9(4):1285–1289.
40. Dicken MJ, et al. (2008) Electrooptic modulation in thin film barium titanate plasmonic interferometers. *Nano Lett* 8(11):4048–4052.
41. Wurtz GA, Pollard R, Zayats AV (2006) Optical bistability in nonlinear surface-plasmon polaritonic crystals. *Phys Rev Lett* 97(5):057402.
42. Gerton JM, Wade LA, Lessard GA, Ma Z, Quake SR (2004) Tip-enhanced fluorescence microscopy at 10 nanometer resolution. *Phys Rev Lett* 93(18):180801.
43. Raschke MB, et al. (2005) Apertureless near-field vibrational imaging of block-copolymer nanostructures with ultrahigh spatial resolution. *ChemPhysChem* 6(10):2197–2203.
44. Sun YG, Xia YN (2002) Large-scale synthesis of uniform silver nanowires through a soft, self-seeding, polyol process. *Adv Mater* 14(11):833–837.
45. Johnson PB, Christy RW (1972) Optical-constants of noble-metals. *Phys Rev B* 6(12):4370–4379.

APPLIED PHYSICAL SCIENCES